





Increased contribution of biomass burning to haze events in Shanghai since China's clean air actions

Wenzheng Fang ^{1✉}, Nikolaos Evangeliou², Sabine Eckhardt ^{2✉}, Ju Xing¹, Hailong Zhang³, Hang Xiao⁴, Meixun Zhao ^{3✉} & Sang-Woo Kim ⁵

High levels of East Asian black carbon (BC) aerosols affect ecological and environmental sustainability and contribute to climate warming. Nevertheless, the BC sources in China, after implementing clean air actions from 2013–2017, are currently elusive due to a lack of observational constraints. Here we combine dual-isotope-constrained observations and chemical-transport modelling to quantify BC's sources and geographical origins in Shanghai. Modelled BC concentrations capture the overall source trend from continental China and the outflow to the Pacific. Fossil sources dominate (~70%) BC in relatively clean summer. However, a striking increase in biomass burning (15–30% higher in a fraction of biomass burning compared to summer and 2013/2014 winter), primarily attributable to residential emissions, largely contributes to wintertime BC (~45%) pollution. It highlights the increasing importance of residential biomass burning in the recent winter haze associated with >65% emissions from China's central-east corridor. Our results suggest clearing the haze problem in China's megacities and mitigating climate impact requires substantial reductions in regional residential emissions, besides reducing urban traffic and industry emissions.

¹Key Laboratory of Geographic Information Science, Ministry of Education, School of Geographic Sciences, East China Normal University, Shanghai 200241, China. ²Department of Atmospheric and Climate Research, Norwegian Institute for Air Research, NILU, Instituttveien 18, Kjeller 2007, Norway. ³Frontiers Science Center for Deep Ocean Multispheres and Earth System, and Key Laboratory of Marine Chemistry Theory and Technology, Ministry of Education, Ocean University of China, Qingdao 266100, China. ⁴Center for Excellence in Regional Atmospheric Environment, and Key Laboratory of Urban Environment and Health, Institute of Urban Environment, Chinese Academy of Sciences, Xiamen 361021, China. ⁵School of Earth and Environmental Sciences, Seoul National University, Seoul 08826, South Korea. ✉email: wzfang@geo.ecnu.edu.cn; sabine.eckhardt@nilu.no; maxzhao@ouc.edu.cn

P_{M2.5} (particulate matter with aerodynamic diameter $\leq 2.5 \mu\text{m}$), a main air pollutant in China with incredibly high concentrations ($\geq 100 \mu\text{g m}^{-3}$) in megacities, has well-documented detrimental impacts on human health^{1–4}. Since clean air actions were established after severe haze incidents in 2013, the annual mean $\text{PM}_{2.5}$ concentrations in China have declined by approximately 30% from 2013 to 2017 ref. 5–8. However, changes in the source contributions of carbonaceous aerosols remain unclear. During the winter months (December–January–February) of 12.2018–02.2020 (before the interference from covid-19 lockdown), severe pollution (daily mean $\text{PM}_{2.5} \geq 100 \mu\text{g m}^{-3}$) still frequently re-occurred in North, Central and East China⁹ (for the time series of $\text{PM}_{2.5}$ levels in Shanghai and other cities, see Supplementary Figs. 1 and 2). Consistent with high $\text{PM}_{2.5}$ concentrations, satellite-based aerosol optical depth (AOD; Fig. 1a) depicts a unique pollution belt shrouding China’s densely populated north-central-east corridor, where the megacity Shanghai – one of the most populous cities in the world (with a population of ~ 25 million) – is located in the downstream belt when northwesterly winds prevail. This persistent haze is a premier challenge to reach the United Nations’ Sustainable Development Goals (SDGs) due to its severe impacts on air quality, regional climate, food security and ecological resources^{10–13}. Shanghai is expected to become a model for sustainable city development in China, within which Chongming Island is being planned, designed and constructed towards a world-class ecological island (for more information on Chongming Island, see Supplementary Note 1). However, achieving such SDGs remains a challenge partly due to unpredictable air pollution and large uncertainties concerning the source contributions and geographic origins.

Carbonaceous aerosols – including elemental (EC, a commonly used mass analogue of BC; hereafter, BC is used for EC) and organic carbon (OC) – are major $\text{PM}_{2.5}$ components in China^{2,14–17}. BC, an indicator of primary anthropogenic emissions formed exclusively from the incomplete combustion of fossil fuels and biomass, strongly absorbs solar radiation and contributes substantially to a positive radiative forcing on the global climate^{18–21}. A significant fraction of OC is water soluble (WSOC; ~ 30 to 80% of OC in East Asia)^{22–24} and absorbs moderate sunlight, thus affecting the climate through direct aerosol-radiation interactions and indirect heating/evaporation of clouds^{21,22,25}. The climate-driven conducive weather patterns may also promote frequent haze formation⁹. However, identifying sources (e.g., BC and WSOC) and reducing regional high anthropogenic emissions is urgent and fundamental to protect human health and limit climate impact^{11,18–25}. Atmospheric chemical transport models – key to examining geographical source regions and validating emission inventories (EIs) used in mitigation and climate models – have been used in simulating BC in the Arctic atmosphere^{26–28}.

Megacities like Shanghai have sought various strategies to fight air pollution^{2,5–8,29}, yet these measures do not seem enough to control the recurrence of aerosol pollution^{1,2,6,17,22}. Observational $\delta^{13}\text{C}/\Delta^{14}\text{C}$ -based methodologies can constrain the sources of BC^{22,30,31} and WSOC^{22–24} in a changing atmosphere. However, after stringent emission controls, such measurements are scarce and rarely extend over the seasonality for East China. A lack of scientific understanding of BC sources and geographical origins hamper practical mitigation efforts on the haze problem on China’s east coast and climate warming. To unveil changes in source contributions and their potential geographic origins, particularly for haze events, we here present a dual-isotope study of BC and WSOC in $\text{PM}_{2.5}$ on the Chongming Island (in Yangtze River Estuary (YRE)) of Shanghai, covering four seasons from December 2018 to November 2019. The radiocarbon signature

($\Delta^{14}\text{C}$) of a sample allows quantifying the proportion of BC (or WSOC, total carbon (TC)) originating from biomass burning (or biomass for WSOC and TC) (containing modern ^{14}C) and fossil (devoid of ^{14}C) sources with high resolution^{22,23,28,31}. The $\delta^{13}\text{C}$ combined with $\Delta^{14}\text{C}$ could further distinguish liquid fossil vs. coal in BC^{22,28,30,31}. For the first time in East Asia, to our knowledge, such BC observations are coupled with FLEXPART (FLEXible PARTicle dispersion)^{26,32} model results driven by global anthropogenic BC and open-fire emissions to quantify the sources and their geographical contributions. We find that trans-province aerosol transport plays an important role in wintertime BC pollution in the Shanghai area, with residential biomass burning bearing the single most significant contributor.

Results

Seasonally varying concentrations of carbon aerosols. The observed BC levels on suburban Chongming Island (YRE; hereafter, the reports focus on YRE unless the urban site is mentioned) displayed large temporal variability and were most pronounced (BC: 0.6 to $7.7 \mu\text{g m}^{-3}$; Supplementary Table 1) in winter (BC and TC month-mean levels shown in Fig. 1b, c and BC levels for all samples shown in Fig. 2a). FLEXPART model results suggest that these large oscillations are connected to geographical air mass origin shifts, with footprints originating northwest from the site dominating high loadings. In contrast, the southeast or ocean footprint was typically clean (Fig. 3 and Supplementary Fig. 3). Apart from the ratio of maxima/minima being larger than 1.5, monthly-mean aerosol concentrations showed a clear seasonal pattern for BC and TC (Fig. 1b, c). The evolution of BC (1.2 ± 0.5 ($n = 12$) to 4.2 ± 2.0 ($n = 6$) $\mu\text{g m}^{-3}$) and TC (4.3 ± 1.9 ($n = 3$) to 15.0 ± 7.0 ($n = 6$) $\mu\text{g m}^{-3}$) monthly-mean concentrations are coincidentally similar to emission trends estimated by previous bottom-up EI in China¹⁴, in which carbonaceous aerosol emissions descend from winter-spring-summer while ascending from summer-autumn-winter.

Higher than $75 \mu\text{g m}^{-3}$ of $\text{PM}_{2.5}$, the maximum allowed daily level in China’s ambient air standard (5 times higher than the new WHO safety guideline)³, frequently occurred at YRE, with peaks of $\sim 200 \mu\text{g m}^{-3}$ in winter (Supplementary Fig. 1). The identical monthly-mean concentrations of both $\text{PM}_{2.5}$ and its composition (e.g., BC, TC) between urban and YRE sites may indicate homologous sources for the Shanghai area. Moreover, there are significant correlations (R^2 : 0.61 – 0.86) between carbon concentrations (TC, BC, WSOC and OC) and $\text{PM}_{2.5}$ levels for both YRE and urban Shanghai sites (Supplementary Fig. 4), suggesting that carbonaceous aerosol is the main $\text{PM}_{2.5}$ component. Specifically, OC was strongly correlated with BC in respective YRE and urban sites (Supplementary Fig. 5), indicating that OC and BC may share common sources (fossil fuel vs. biomass burning) in respective YRE and urban. The observed wintertime BC ($3.5 \pm 2.0 \mu\text{g m}^{-3}$, $n = 22$) and WSOC ($7.9 \pm 3.9 \mu\text{g m}^{-3}$, $n = 22$) concentrations were higher than previous observations in the 2013–2014 winter in Shanghai (e.g., $3.0 \mu\text{g m}^{-3}$ from ref. 17, $1.7 \pm 0.7 \mu\text{g m}^{-3}$ from ref. 22) and in January 2013 in Zhejiang (neighbouring province)^{30,31}, although slightly lower than the 2013–2014 winter haze in Tianjin and Beijing^{22,24,30,33}. The elevated OC/BC ratios (in the range of 3–4) in winter may be a rough indicator of the high contribution of biomass burning and secondary aerosol formation (SOA)^{19,22,31}. Conversely, the lower OC/BC ratios in summer (~ 2) may roughly indicate a relatively higher contribution from fossil fuel combustion and primary sources^{19,22,31,33}. However, these inferences cannot quantify source contributions due to high uncertainties in emission factors (i.e., BC and OC) and the complicated influence of SOA^{14–16,19,22,31,34,35}.

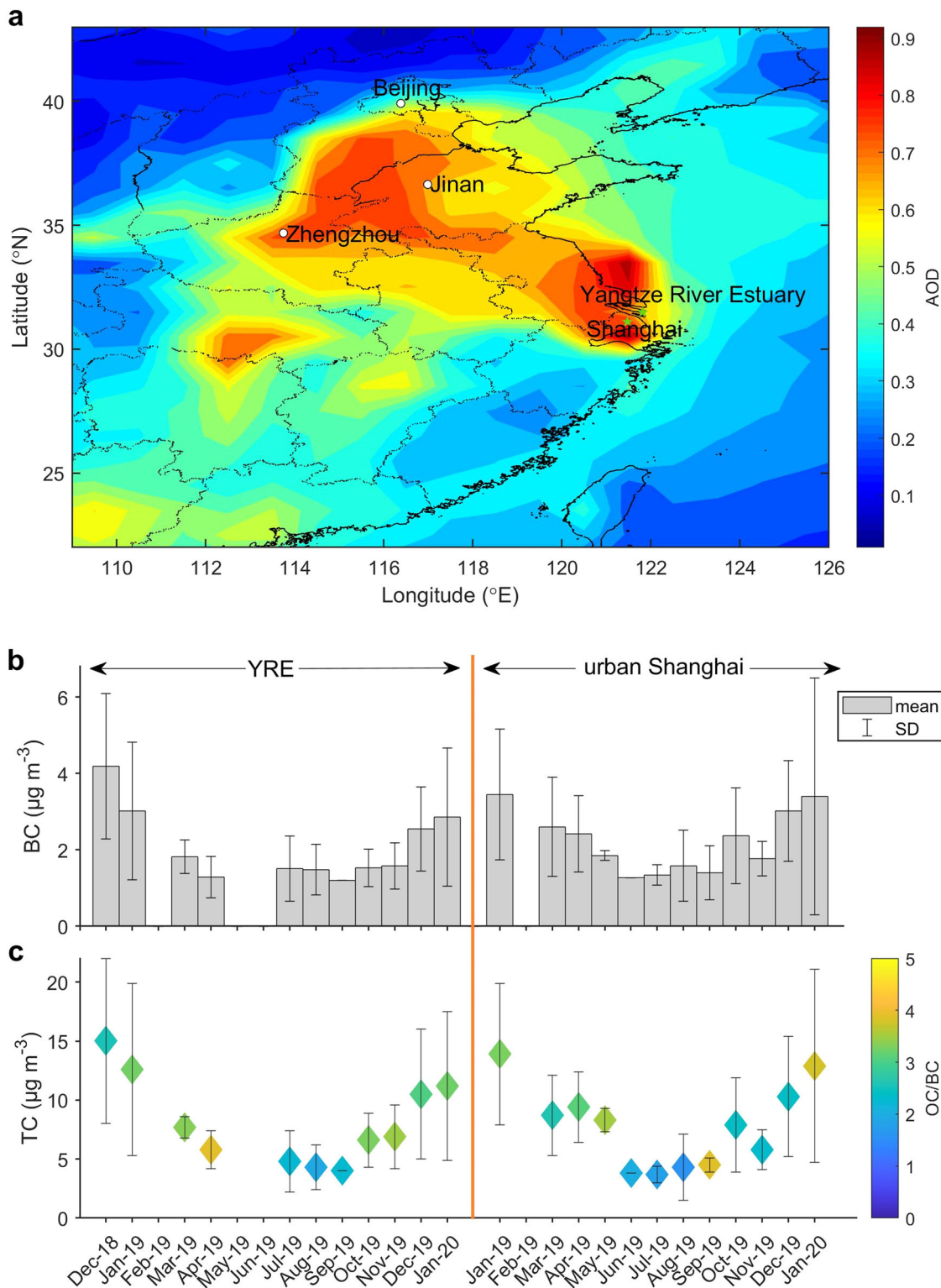


Fig. 1 Shanghai and Yangtze River Estuary (YRE) locations, geographical distributions of aerosol optical depth (AOD), concentrations and OC-to-BC ratios. **a** Sampling sites (green stars) in urban Shanghai and suburban receptor YRE and AOD (550 nm) showing high aerosol loadings over central-east China from Dec-2018 to Jan-2020. The circles denote three other major upwind cities. **b, c** Monthly mean variability in both concentrations of BC and TC (with OC-to-BC ratios) in PM_{2.5} over YRE and urban Shanghai (sampling dates and times are provided in Supplementary Table 1). The error bars in (**b, c**) denote the SD of observed data. The colour bar in (**c**) indicates OC/EC fraction for each month at each location. The no-data months in (**b, c**) are due to no sampling in those months. AOD data were obtained from NASA Moderate Resolution Imaging Spectroradiometer (MODIS) level 3 collection 6.

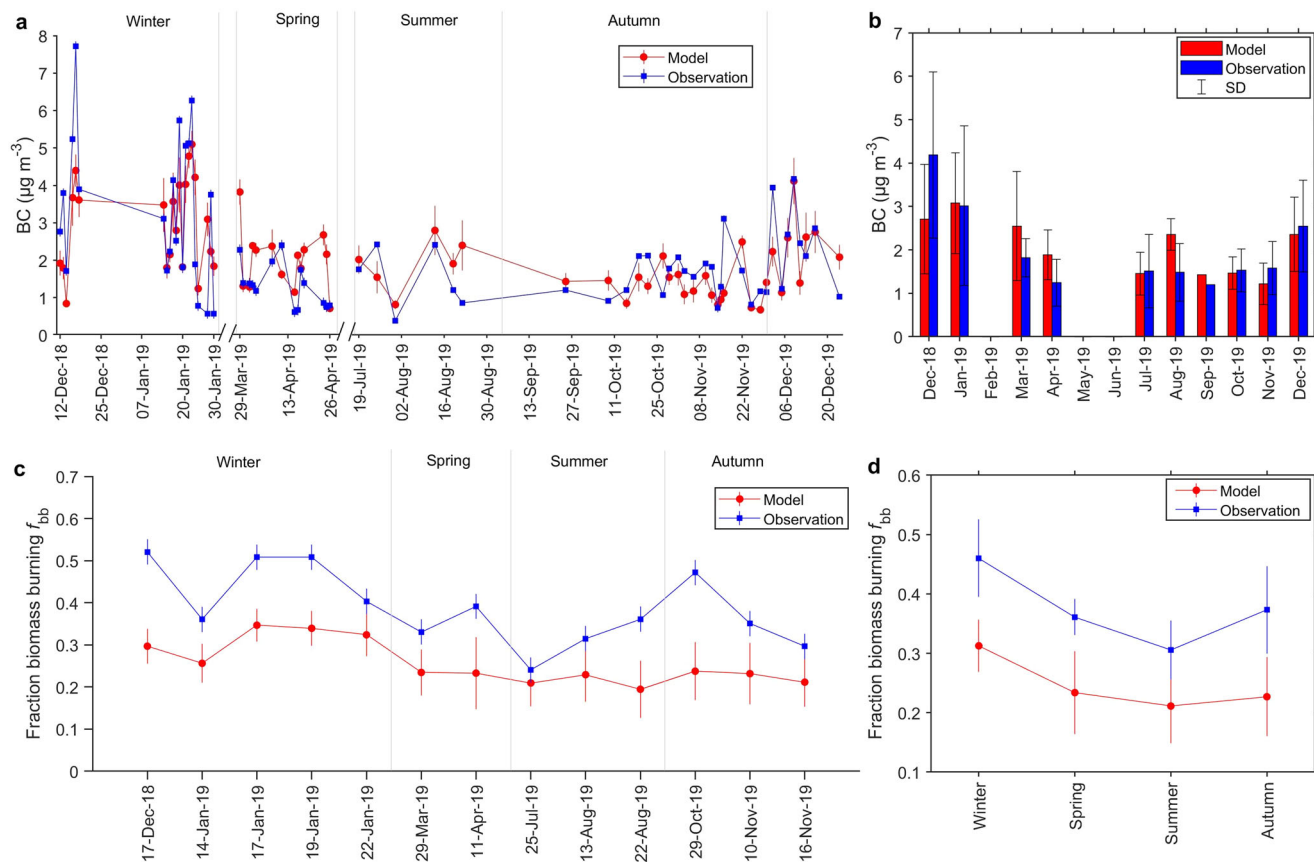


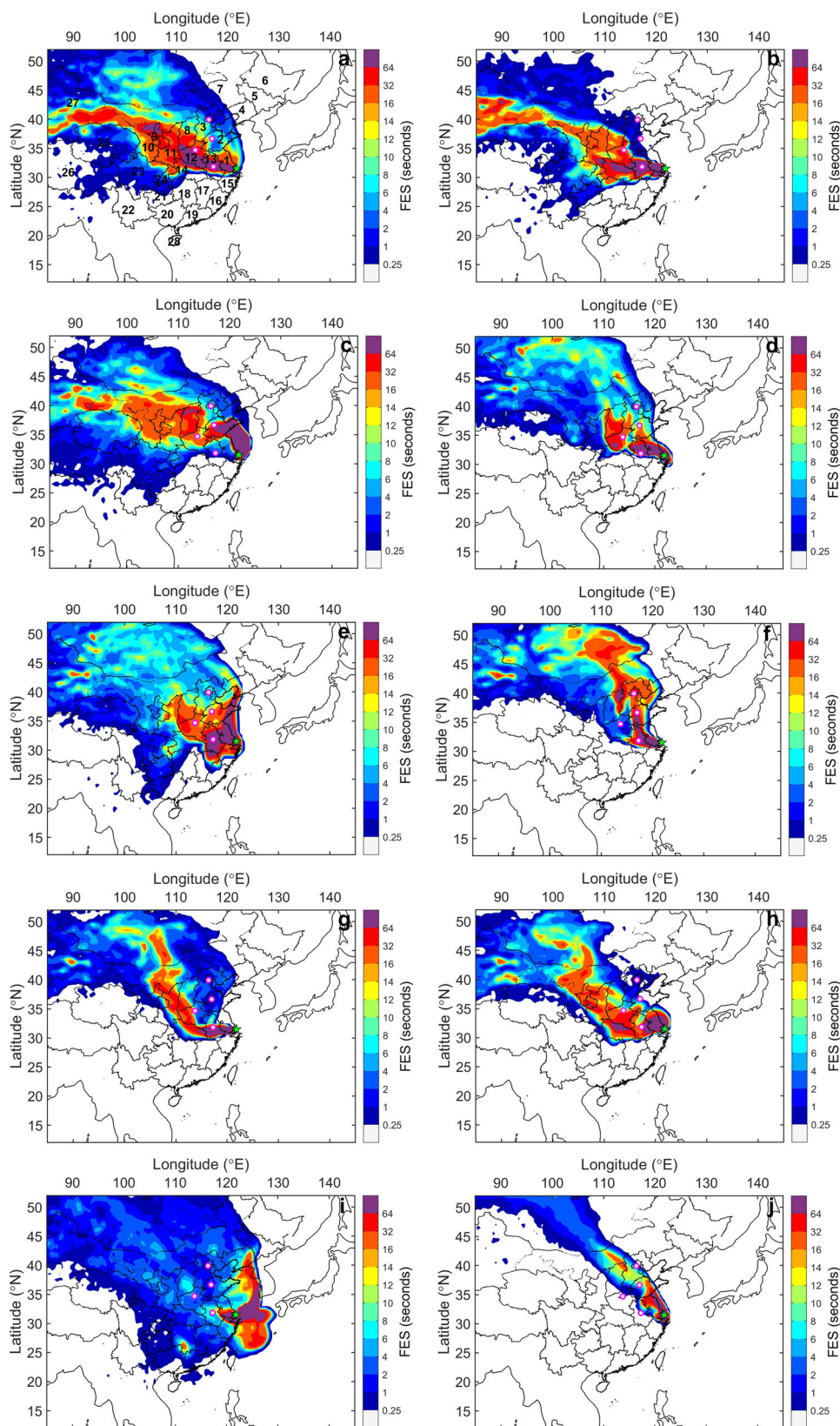
Fig. 2 Observation-model comparison of BC concentrations and fraction of biomass burning (f_{bb}) of BC in the YRE site. Blue squares (or bars) and red circles (or bars) show observed and modelled results, respectively. **a** BC concentration comparisons between observed and modelled results for time series of PM_{2.5} samples. The break on the x-axis means a period with no sampling. **b** Observation-model comparisons of monthly-mean BC levels for all samples collected in this study. The no-data months are due to no sampling in February, May and June in the YRE. Observation-model comparisons of **(c)** f_{bb-BC} of selected isotope samples and **(d)** seasonal-mean BC sources for isotope samples. The f_{bb} for top-down observations was based on the ¹⁴C analysis, while modelled f_{bb-BC} was calculated based on FLEXPART-ECLIPSE-GFED (FEG) coupling. The times in **c** are only used to refer to each sample and its corresponding sampling start date. Error bars in **(a, c)** correspond to uncertainties of observations and the SD of modelled results. Error bars in **(b, d)** are the SD of monthly and seasonal means for observed and modelled results.

Source apportionment using carbon isotopes and MC model.

The signature of radiocarbon $\Delta^{14}\text{C}$ and stable $\delta^{13}\text{C}$ offers direct insight into the relative contribution from major emission source categories. Here we find a clear seasonality in the $\Delta^{14}\text{C}$ of BC (Fig. 4a), with a high fraction of biomass burning (f_{bb} ; equation (1) in Method) in the polluted winter (up to 52%) yet a lower f_{bb} (down to 24%) in the relatively clean summer. The observed f_{bb-BC} values fluctuate between and within seasons (Fig. 2c), revealing inter- and intra-seasonal source variability. Nevertheless, the seasonal means of f_{bb-BC} values show a clear cycle over the year at YRE, decreasing from the highest f_{bb-BC} in winter ($45 \pm 7\%$, $n = 5$) over spring ($36 \pm 3\%$, $n = 2$) to the lowest f_{bb-BC} ($31 \pm 5\%$, $n = 3$) in summer and increasing from summer to autumn ($37 \pm 7\%$, $n = 3$) (Fig. 2d and Supplementary Table 2). Intriguingly, the high f_{bb-BC} values were also observed in winter haze at the urban site ($\sim 40\%$ ($n = 3$); Fig. 4c), suggesting a similar source regime extending over a large area. The slightly lower urban f_{bb-BC} values are likely due to the proximity of the fossil vehicle emissions. The current wintertime f_{bb-BC} values ($45 \pm 7\%$, $n = 5$) had a higher biomass burning fraction than those reported for the few previous studies in East Asia, for example, $22 \pm 3\%$ ref. 22 for both Shanghai and Beijing in January 2014 (Fig. 4c), Beijing ($25 \pm 8\%$)³³ and Tianjin (in North China; $27 \pm 2\%$)³⁰ in January 2013, Shanghai ($25 \pm 8\%$)³³ and Zhejiang (in Yangtze River Delta (YRD); $33 \pm 3\%$)³¹ in January 2013. However, they were comparable to the Sichuan basin in

autumn 2012 and spring 2013 ($48 \pm 8\%$)³¹ and the South Asian megacity Delhi in winter 2011 ($43 \pm 17\%$)³⁶. The rising f_{bb-BC} observed in Shanghai in East China is likely a result of several combined processes: (i) residential biofuel emissions are enormous, scattered and fuel-changeable^{5,9,12,14,15}, (ii) aggressive air pollution controls focus on power, industry and transport, resulting in considerably declined fossil-fuel emissions^{4-8,15}, (iii) disparities of China's emission control for different regions, e.g., stringent emissions controls were preferentially enacted in developed regions compared to the small cities and rural areas^{5-8,22,29,31}, (iv) reshaping the energy system and setting a cap for provincial coal consumption to control fossil fuel emissions^{5-8,37,38}, which may impact the available fuel types (i.e., coal) used in residential and commercial and (v) enhanced air pollution transported⁹ from regions carrying high f_{bb-BC} to YRE in the current winter compared to earlier²² observed lower loadings in Shanghai (e.g., back trajectories suggest the Jan-2014-Shanghai study²² intercepted northern continent air diluted with ocean air, see Supplementary Fig. 6).

In addition to radiocarbon, $\delta^{13}\text{C}$ of inert BC (retain $\delta^{13}\text{C}_{BC}$ signature during atmospheric processing, as opposed to OC) adds a dimension for three primary sources: biomass, liquid fossil and coal^{22,30,31} (for source endmembers, see Supplementary Table 3). A Monte Carlo approach (MC; Methods) is employed to account for the variability in $\delta^{13}\text{C}$ and $\Delta^{14}\text{C}$ of both samples and source endmembers, thus allowing a statistical source apportionment for



YRE and urban Shanghai. The MC results for f_{bb-BC} (Fig. 5a and Supplementary Table 4) are identical to those acquired from $\Delta^{14}C$ directly (Fig. 2c). The most important information provided by the MC model is the further deconvolution of fossil fraction into coal (f_{coal}) and liquid fossil fuel ($f_{liq.fossil}$). The highest coal-burning contribution (31–33%, Fig. 5a) simulated by the MC

model in all samples coincides with the two most enriched $\delta^{13}C-BC$ signatures ($-25.1 \pm 0.1\text{‰}$ and $-24.8 \pm 0.1\text{‰}$; Fig. 4a) observed in winter (14-Jan-2019) and autumn (29-Oct-2019), with an overlapping footprint from North China (Fig. 3c, j). In contrast, the lowest coal-burning contribution (17–20%) coincides with the three most depleted $\delta^{13}C-BC$ values ($\leq -26.5\text{‰}$)

Fig. 3 FLEXPART potential footprint emission sensitivity (FES) to YRE for representative samples. BC aerosol FES arrived at YRE, Chongming Island site (green star). Winter pollution (**a–h**), the most depleted $\delta^{13}\text{C}_{\text{BC}}$ (**i**; spring) and most enriched $\delta^{13}\text{C}_{\text{BC}}$ (**j**; autumn) samples. **a** Model output for sample CM4, 16-Dec to 17-Dec, 2018. **b** Model output for isotope sample (BC, WSOC) CM5, 17-Dec to 18-Dec, 2018. **c** Model output for isotope sample (BC, WSOC) CM7, 14-Jan to 15-Jan, 2019. **d** Model output for isotope sample (BC, WSOC) CM10, 17-Jan to 18-Jan, 2019. **e** Model output for isotope sample (BC, WSOC) CM12, 19-Jan to 20-Jan, 2019. **f** Model output for sample CM14, 21-Jan to 22-Jan, 2019. **g** Model output for isotope sample (BC, WSOC) CM15, 22-Jan to 23-Jan, 2019. **h** Model output for isotope sample (WSOC) CM16, 23-Jan to 24-Jan, 2019. **i** Model output for isotope sample (BC, WSOC) CM22, 29-Mar to 30-Mar, 2019. **j** Model output for isotope sample (BC) CM48, 29-Oct to 31-Oct, 2019. #1–28 on the map (**a**) denotes some provinces in mainland China: Jiangsu, Shandong, Hebei, Liaoning, Jilin, Heilongjiang, Nei Mongol, Shanxi, Ningxia, Gansu, Shaanxi, Hainan, Anhui, Hubei, Zhejiang, Fujian, Jiangxi, Hunan, Guangdong, Guangxi, Guizhou, Yunnan, Sichuan, Chongqing, Qinghai, Xizang, Xinjiang and Hainan. The north-to-south circles represent city Beijing, Jinan, Zhengzhou and Hefei, respectively.

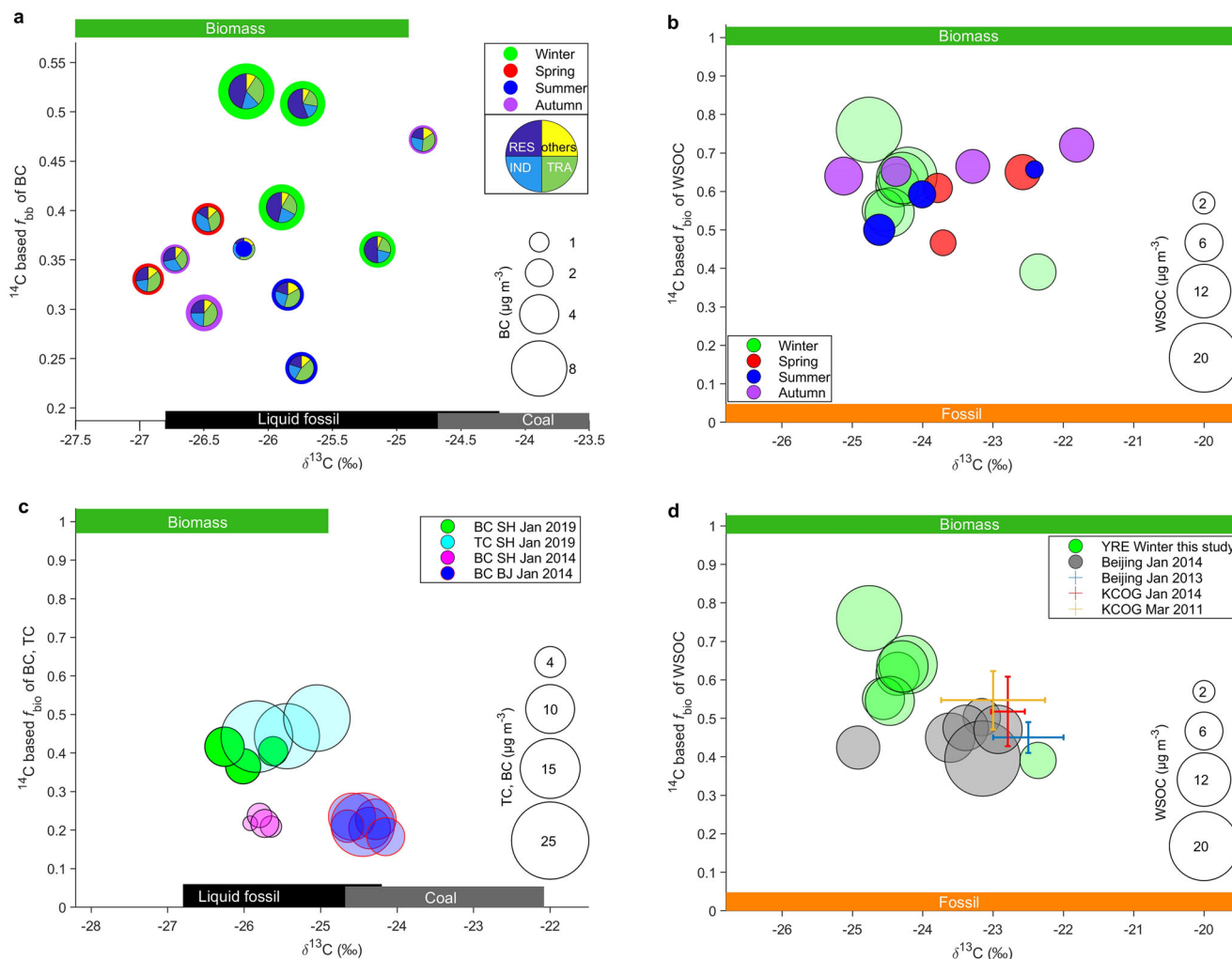


Fig. 4 Multi-dimensional source apportionment. The expected $\Delta^{14}\text{C}$ and $\delta^{13}\text{C}$ endmember range for biomass, liquid fossil, coal and fossil are shown as green, black, grey and orange rectangles, respectively. The circle area shows carbon aerosol (e.g., BC, TC and WSOC) concentrations in $\mu\text{g m}^{-3}$ (see scales with black circles on the bottom-right side). **a** Seasonal isotope signatures of BC at YRE, showing as a doughnut or shading circle. The pie charts show sectoral contributions simulated by the FEG coupling (that is, residential, transport, industry and others). **b** Seasonal variations of isotope signatures of WSOC at YRE. **c** Isotope signatures of BC and TC for urban Shanghai during the current Jan-2019 study compared to earlier observation for Shanghai and Beijing in Jan-2014 ref. ²². **d** Isotope signatures of WSOC during the current winter YRE study (Dec-2018 to Jan-2019) compared to earlier reported data for winter Beijing (2013 ref. ²⁴, 2014 ref. ²²) and KCOG (Korea Climate Observatory at Gosan; 2011 ref. ²³, 2014 ref. ²²). Uncertainties are typically less than 0.2‰ for $\delta^{13}\text{C}$ and 5‰ for $\Delta^{14}\text{C}$ (corresponding to <1% for f_{bb}) and thus not shown here because they are much smaller than the diameter of the circles (all dual-isotope data are provided in Supplementary Table 2). Note the small scale for f_{bb} of panel (**a**) (in order to make the pie chart visible/readable) compared to panels (**c**, **d**).

observed in spring and autumn (Fig. 5a and Supplementary Tables 2 and 4). In addition to the seasonal cycle of $f_{\text{bb-BC}}$, $f_{\text{liq.fossil-BC}}$ exhibits another significant seasonality, increasing from the lowest winter (~30%) to the highest spring and summer (~45%) but decreasing from summer to autumn. Contrary to $f_{\text{liq.fossil-BC}}$

and $f_{\text{bb-BC}}$, no distinct seasonality for the $f_{\text{coal-BC}}$ was observed, but instead, it remained relatively constant between seasons (Fig. 5b). Combining these relative fuel fractions with BC levels provides quantitative concentrations of the three fuels. We find that biomass burning emissions are the dominant driver for

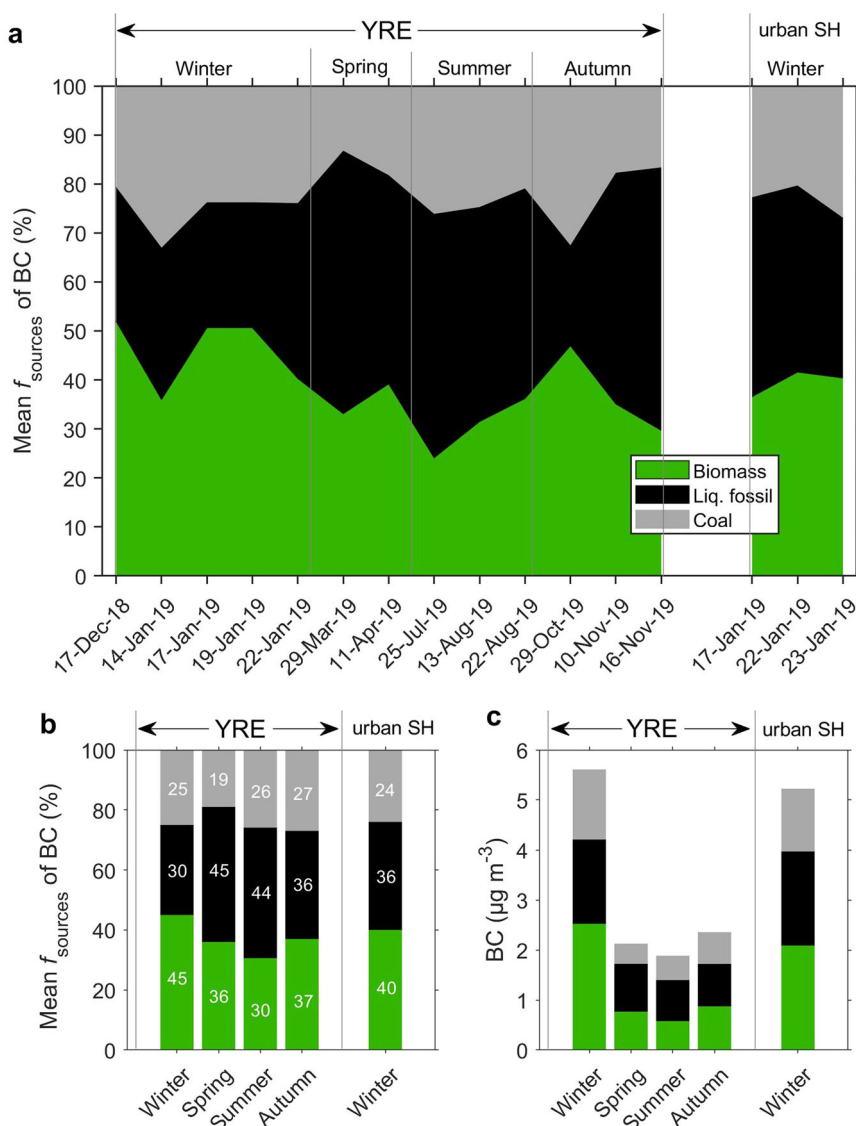


Fig. 5 Dual-isotope-constrained fuel type contributions and seasonal corresponding mean mass concentrations to BC from Monte Carlo (MC) model.

a MC-simulated mean source fractions of biomass, liquid fossil and coal fuel combustion for isotope samples collected in YRE (from Dec-2018 to Nov-2019) and urban Shanghai (Jan-2019). Dates (DD-Month-YY) refer to selected isotope samples and denote the sampling start date of those samples (see Supplementary Tables 1 and 4 for sample details). **b** Seasonally-averaged source fractions in YRE and urban Shanghai winter. **c** The source concentrations to seasonal BC in YRE and urban Shanghai (using mean BC concentration multiplied by the mean fraction of sources for each season). The white gap separates the YRE site (four seasons in turn) and urban SH (Shanghai; only Jan-2019). The SD for data in (a, b, c) are provided in Supplementary Fig. 7.

variation in BC concentrations between winter pollution ($\text{BC}_{\text{bb}} = 2.5 \pm 0.5 \mu\text{g m}^{-3}$) and the relatively cleaner seasons ($\text{BC}_{\text{bb}} = 0.6 \pm 0.2 \mu\text{g m}^{-3}$) over YRE, even though liquid fossil and coal also play a considerable role in the rising wintertime BC levels (Fig. 5c and Supplementary Table 5, all the SDs for the results of Fig. 5 are provided in Supplementary Fig. 7).

Consistent with high $f_{\text{bb-BC}}$ in winter haze, a high fraction of biomass (f_{bio} , biomass means that WSOC and TC may originate from biomass burning and natural biomass emission) was also observed in WSOC (YRE: $f_{\text{bio}} = \sim 60\%$, $10.6 \pm 4.0 \mu\text{g m}^{-3}$, $n = 7$) and TC (urban Shanghai: $f_{\text{bio}} = \sim 46\%$, $21.2 \pm 2.7 \mu\text{g m}^{-3}$, $n = 3$) during the same anthropogenic pollution episodes (Fig. 4), again much higher than earlier observations (e.g., (i) in Beijing in January 2014 ref. 22: $f_{\text{bio}}(\text{WSOC}) = \sim 45\%$, $11.0 \pm 6.0 \mu\text{g m}^{-3}$; $f_{\text{bio}}(\text{TC}) = \sim 30\%$, $39.4 \pm 17.7 \mu\text{g m}^{-3}$. (ii) in Beijing in January ref. 24: $f_{\text{bio}}(\text{WSOC}) = 46 \pm 4\%$, $\sim 10.0 \mu\text{g m}^{-3}$). SOA formed from the oxidation of biogenic VOCs (BVOCs) is unlikely to contribute

to wintertime OC pollution because BVOCs emissions (strongly dependent on temperature and sunlight)³⁹ are much lower under cold temperatures and prevailing northwesterly winds in winter²² (Supplementary Fig. 8), whilst it may play a role in summer-autumn WSOC. Nonetheless, f_{bio} (or f_{bb}) of BC and WSOC still oscillated in a similar monthly trend (Supplementary Fig. 9). Furthermore, the concentration of another biomass-burning marker, potassium, strongly correlated with the concentration of ^{14}C -based biomass content (BC, WSOC and TC; Supplementary Fig. 10), showing biomass burning dominating biomass carbon in $\text{PM}_{2.5}$. Taken together, biomass burning tangles with wintertime aerosol pollution of Shanghai, including not only BC but also other $\text{PM}_{2.5}$ components.

FLEXPART model simulated vs. observed BC. The Lagrangian atmospheric transport model FLEXPART (version 10.4)⁴⁰, coupled with the recently updated ECLIPSE (Evaluating the Climate

and Air Quality Impacts of Short-Lived Pollutants version 6B)¹⁵ EI and open-fire BC emissions⁴¹ from GFED (Global Fire Emission Database version 4)⁴², was used to simulate BC concentrations and source contributions at the YRE site. The FLEXPART-ECLIPSE-GFED (hereafter FEG) modelled BC concentrations match the overall observed values and seasonality remarkably well in China's east coast, YRE (Fig. 2 and Supplementary Fig. 11a, b; $R = 0.72$, $P < 0.05$). The model reproduced the observed BC concentration in the winter haze, with some underestimations that may be related to the uncertainty in the EI (e.g., may be due to underestimation of residential BC emissions and source misallocation for these winter haze samples). The modelled (and observed) peak concentrations re-occurred frequently in winter when the air was predominantly transported from northern and central China to YRE, therefore accumulating BC during air mass transport (Fig. 3a–h). Several highly overestimated concentrations (factor of >2) by the model simulations relative to the observations are likely due to the precipitation during sample collection removing substantial aerosols through wet deposition (Supplementary Fig. 8c). Additionally, the transport of BC into the YRE during the spring-summer monsoon is challenging to model because of the complex precipitation scavenging, resulting in a slight model overestimation. On a monthly/seasonal basis, BC concentrations and cycles are almost identical between the model simulations and observations, which further shows good model performance in capturing the observed strong seasonality (Fig. 2b and Supplementary Fig. 12).

Furthermore, the modelled f_{bb-BC} can be calculated from the FEG coupling (Supplementary Note 2) allowing direct source comparison with the $^{13}C/^{14}C$ -based observational source apportionment. The model performance in the f_{bb-BC} was in good agreement with the observations (Supplementary Fig. 11c; $R = 0.77$, $P < 0.05$), with the model-observation offsets (model underprediction) between 3–15%. The model-simulated seasonality was analogous to the observations but showed consistent underestimation, with the highest f_{bb-BC} during the winter pollution and the opposite during cleaner summer (Fig. 2c, d). We also note that the FEG- f_{bb-BC} oscillated seasonally with BC concentrations (Supplementary Fig. 12; $R = 0.79$ for monthly, $R = 0.99$ for seasonal, $P < 0.05$), with high f_{bb-BC} corresponding to high pollution. Thus, this is consistent with the above $^{13}C/^{14}C$ -based observational insight that biomass burning exacerbates winter haze in Shanghai. Open biomass burning BC was previously tentatively assigned as a major contributor to wintertime BC in Delhi in South Asia³⁶. However, modelled wildfires BC in Shanghai winter is merely a minor contributor ($\sim 1\%$; Supplementary Fig. 13) compared to residential biomass burning ($>30\%$). The enormous residential emissions yet changeable fuel used may be challenging to EI, resulting in being unable to correctly record the source category in EI. The misallocation of residential biofuel use as fossil use or overestimating fossil emissions from other sectors can cause an underestimation in f_{bb-BC} compared to observations. In some of the major BC (EI) emission provinces, the proportion of biofuel-burning derived BC within the residential sector is very low (for example, approximately 23%, 28%, 8% and 10% in Hebei, Henan, Nei Mongol and Shanxi, respectively), which may require EI to verify further. Therefore, an underestimation of biofuel-burning emissions from the densely populated residential likely dominated the offset, consistent with previous model findings that emissions from China's residential areas are a significant and underrated ambient aerosol pollution source^{43,44}.

Geographical and sectoral contributions of BC based on FEG. The FEG coupling simulated both geographical (grid cell) and sectoral contributions to surface BC, allowing investigation of

BC's origin at a provincial level. The present FEG BC footprint emissions indicate inter- and intra-seasonal shifts in the anthropogenic BC arriving at YRE (Fig. 6 and Supplementary Fig. 14), suggesting the central-east corridor (see Fig. 6a) as the major geographical source region during the winter pollution events. Figure 7a, c and Supplementary Fig. 15 quantitatively depict provincial contributions to BC in the high-loading samples, including seasonal isotope analysis samples. During the winter pollution period, the trans-provincial sources contributed overwhelmingly, ranging between 80–96%, with Jiangsu, Anhui, Henan and Shandong contributing $\sim 65\%$ (Fig. 7b, d). North China was also an appreciable source of winter pollution. For example, the FEG coupling suggests high contributions ($\sim 60\%$) from Shandong, Shanxi, Hebei, Nei Mongol and Gansu for a high fossil-coal sample (14 January 2019) that is consistent with expected high coal-burning emissions in these regions. Conversely, the relatively cleaner summer was predominantly affected by local and southeast regions (e.g., Zhejiang, Fujian and Guangdong; Figs. 6b and 7c), where biomass-burning emissions are much lower compared to central-east China, in agreement with the observed lower f_{bb-BC} .

The simulated BC concentrations can be further split into eight sectors, with residential, industry and transport accounting for 76–94% of emissions (Supplementary Fig. 13). The simulated sectoral contributions (the sector contributed BC concentration divided by the total BC concentration) showed distinct seasonality in this study: (i) residential dominated winter ($\sim 50\%$) yet reduced to only 17% in summer, (ii) transport increased vastly from wintertime 22% to the highest (41%) in summer, while the absolute BC concentrations from the transport were almost identical during the seasons, (iii) industry remained relatively constant across seasons and (iv) wildfires had the highest in summer ($\sim 2\%$) relative to other seasons ($\sim 1\%$). Regarding the geographical origins of these sectoral emissions (including residential, transport, industry, energy, waste and wildfires), the provincial contributions by sectors displayed high diversity over the study year (for seasonal province contributions of residential, transport and industry BC, see Fig. 8 and Supplementary Figs. 16–18; for province contributions of residential, transport and industry BC during winter haze, see Supplementary Fig. 19; for seasonal province contributions of waste-burning, energy and wildfires BC, see Supplementary Figs. 20–22). Jiangsu, Anhui, Henan and Shandong together were responsible for $>60\%$ of residential emissions in winter haze, whereas the remaining mainly was from Shanxi, Hebei, Hubei and Shanghai (Fig. 8a, d and Supplementary Fig. 19a, d). Jiangsu, Zhejiang and Shanghai dominated industry BC across four seasons (Fig. 8c, f), yet the north-central-east pollution belt also significantly supplied the winter pollution (Supplementary Fig. 19c, f). In contrast, another large BC contributor, transportation, was uniformly predominant from Shanghai and neighbouring Jiangsu and Zhejiang across the year (Fig. 8b, e and Supplementary Fig. 19b, e). Additionally, Jiangsu, Shanghai and Anhui stood up $>70\%$ of the minor contributors of waste and energy (Supplementary Figs. 20, 21), while another negligible emission of open fires originated from widespread regions (Supplementary Fig. 22).

Discussion

Understanding changes in sources and levels of carbonaceous aerosols and geographical contributions is imperative for policymakers concerned with air quality, sustainable development, and near-term climate change. The quantitative isotope-based source apportionment of BC (and WSOC and TC) reveals that the relative contribution of biomass burning emissions is

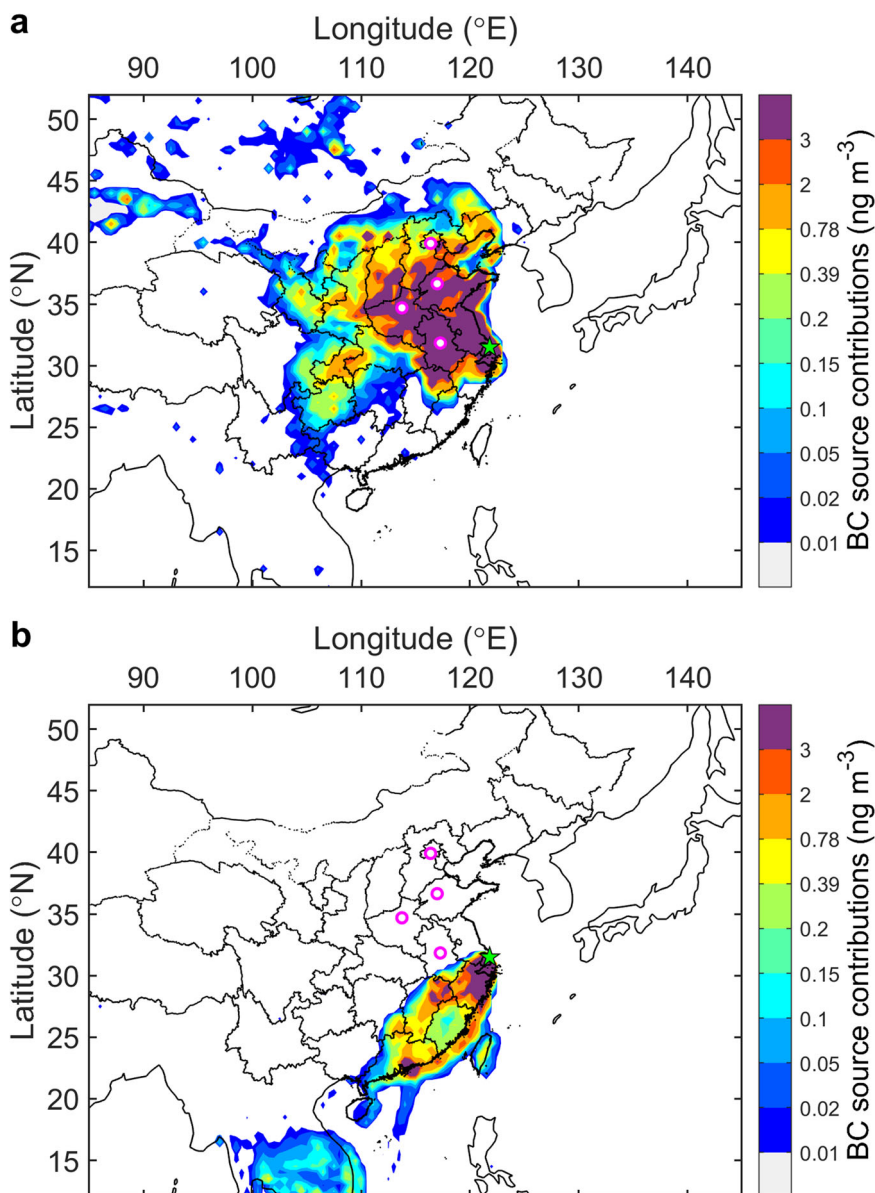


Fig. 6 FLEXPART-simulated geographical distribution of anthropogenic BC source contribution to the simulated mixing ratio at YRE (Chongming Island, green star) for representative winter and summer samples. Anthropogenic BC source contribution comprises sectors of residence, industry, transport, energy, waste, open fire (open biomass burning), and ship and gas flaring. Model output for (a) winter isotope sample CM12, 19-Jan to 20-Jan, 2019 and (b) summer isotope sample CM37, 25-Jul to 28-Jul, 2019. The north-to-south circles represent the cities of Beijing, Jinan, Zhengzhou and Hefei, respectively.

increasing in Shanghai winter air pollution (~45%) compared to previous observations in January 2013/2014 in Shanghai (and other cities in YRD) and the Beijing-Tianjin-Hebei region (~20%)^{22,30,31,33}. Our results highlight the increasing importance of residential biomass burning emissions under the current emission controls, with FEG coupling suggesting principally from central-east China. As regards the FEG coupling, our observations imply that EIs underestimate biofuel burning, suggesting the need for improvement in the vast small-scale but highly changeable residential emissions in China's populated countryside.

Megacities such as Shanghai have implemented measures to curb traffic and industry emissions, for instance, transferring some high-polluting enterprises out of the city, on working days only allowing motor vehicles that bought expensive local licenses and local electric vehicles to drive on the central and inner ring Expressways (overhead viaduct). However, vehicle restrictions

may also have considerable uncertainty on vehicle emissions; for example, road restrictions of the central and inner Expressways may lead non-local licensed vehicles to opt for ground driving routes (which are usually more congested in urban areas), increasing ground traffic congestion and, thus, inducing higher emissions. In contrast, using more electric vehicles and subways to reduce transport emissions would decrease local fossil vehicle emissions and be propitious to improve air quality.

Despite a rapid energy transition in China, residential solid fuels are still used extensively in rural areas, particularly for heating and cooking, contributing significantly to air pollution and population exposure^{5,14-16,19,43,44}. Rural residential emissions affect both rural and urban air quality, and the impacts are highly seasonal- and location-dependent. Future opportunities for controlling PM_{2.5} emissions may exist in the rural residential sector and small industries (for example, the small boiler and

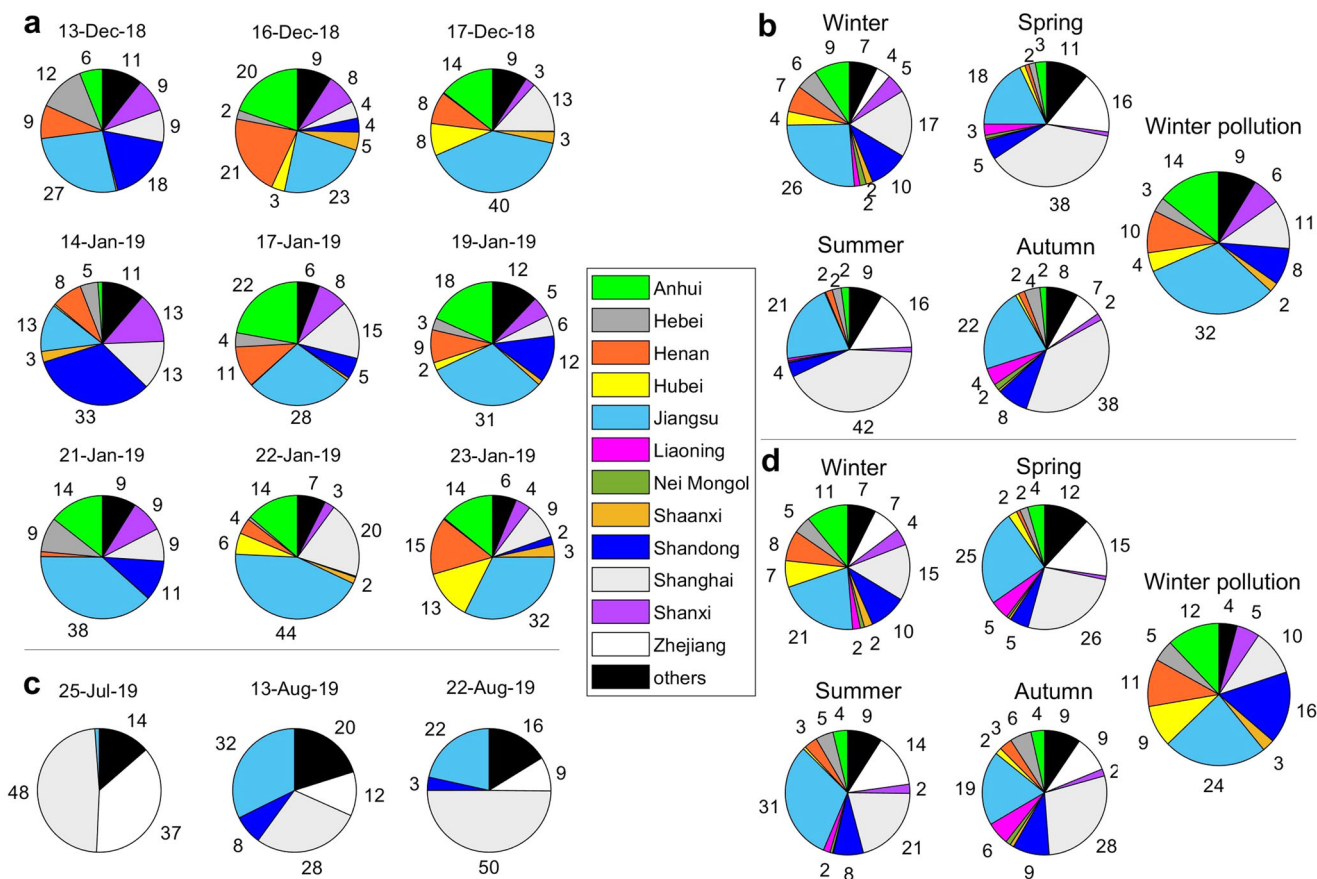


Fig. 7 Contrasting province contributions to BC at YRE in winter haze and other seasons based on FEG simulations. The number in the pie chart represents the percentage. Province contribution means a mass fraction of BC contributed by the province to YRE site. **a** Model output for winter samples, including samples: 13-Dec-2018 (CM2), 16-Dec-2018 (CM4); isotope samples: 17-Dec-2018 (CM5; $BC_{bb}({}^{14}C\text{-based observation}) = 3.5 \mu g m^{-3}$), 14-Jan-2019 (CM7; $BC_{bb} = 1.4 \mu g m^{-3}$), 17-Jan-2019 (CM10; $BC_{bb} = 1.9 \mu g m^{-3}$), 19-Jan-2019 (CM12; $BC_{bb} = 2.6 \mu g m^{-3}$); sample 21-Jan-2019 (CM14); isotope sample 22-Jan-2019 (CM15; $BC_{bb} = 2.3 \mu g m^{-3}$) and sample 23-Jan-2019 (CM16). **b** Seasonal province contributions to BC. The seasonal calculations include all samples in the current campaign, while the ‘winter pollution’ calculations only count on high-loading samples shown in (a). **c** Model output for summer isotope samples 25-Jul-2019 (CM37; $BC_{bb} = 0.7 \mu g m^{-3}$), 13-Aug-2019 (CM39; $BC_{bb} = 0.7 \mu g m^{-3}$) and 22-Aug-2019 (CM41; $BC_{bb} = 0.3 \mu g m^{-3}$). **d** The SD for data shown in (b). The sectors in province contribution calculations comprise residence, industry, transport, energy, waste and open fire (open biomass burning). The contribution of gas flaring was negligible ($\sim 0.1\%$ of total BC concentration) and it was excluded from this calculation. Shipping emissions dominated in the nearby ocean (they were also excluded from this calculation) and could not affect province contribution calculations due to their minor contributions to total BC concentrations (typically around 1%).

brick production) by replacing solid biofuels (and coal) with cleaner stoves – whose emissions in BC and other aerosols are none or less. Cleaner energies, with regard to particle emissions, such as natural gas (NG), liquid petroleum gas (LPG) and electricity, are potential mitigation options in the residential sector^{45,46}. Nevertheless, China’s NG pipeline network to supply residential gas fuel does not cover large rural areas^{45–47}. On the other hand, the energy guideline in the residential sector requires careful management. It needs to consider trade-offs between air quality and affordability of residents since gas and electricity are expensive for heating and cooking for low-income residents^{10,47}. Another promising option is to speed up the filtration of burning plumes, which removes particles from the stove burning.

The ubiquitous winter haze affects hundreds of millions in central and east China while confounding city dwellers and policymakers about its source. East Asian megacities are important sources of regional air pollution, but it is often overlooked that they may also be receptors affected by the transport of upstream pollutants. Here we find that trans-province aerosol transport plays an essential role in the current Shanghai winter-time BC pollution study, with residential emissions bearing the

single most significant contributor, followed by transportation and industry, yet wildfires may contribute insignificantly in the study period. The air pollution transport could exacerbate the megacity haze and offset its efforts to control traffic emissions. Thus, regional haze governance requires local governments to formulate tailored emission reduction measures and inter-provincial coordinated haze control, joint prevention and control and vertical environmental protection management.

This year-round dual-isotope-based observations and chemical transport modelling provide a more accurate assessment of current sources in the YRE and a scientific underpinning to practical and effective mitigation toward the largest sources of carbon aerosols. Drastically cutting residential biomass burning in central-east China and reducing vehicle/industrial emissions through urban efforts is required to improve air quality and mitigate climate impact in Shanghai and East Asia. Our findings provide the first understanding of province-level-contribution year-long BC sources arriving in Shanghai, which can be compared to the past and future measurements of these changing anthropogenic emissions. The approaches that combined the isotope-based observation and chemical transport modelling in this study can be applied to

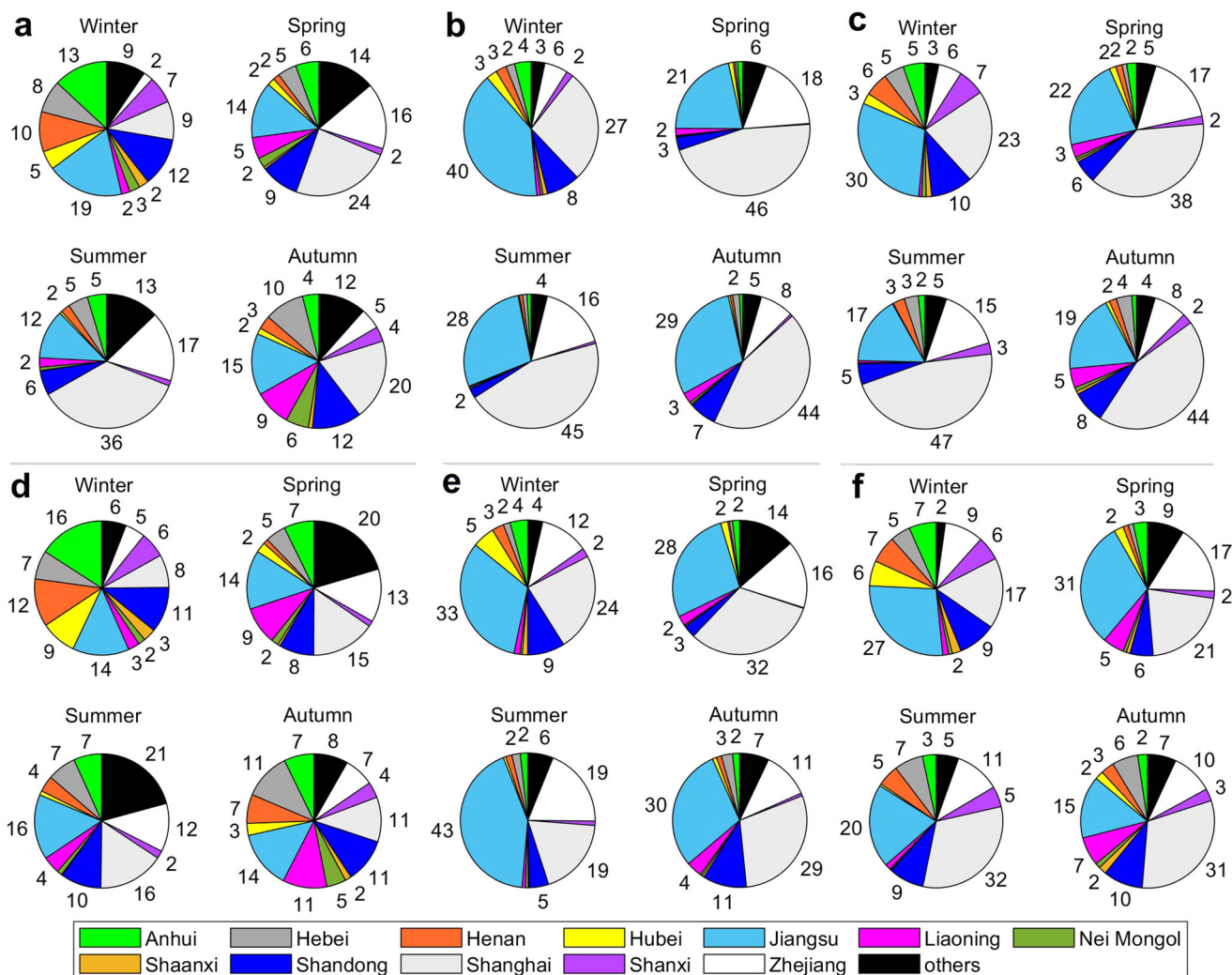


Fig. 8 Seasonal province contributions of residential, transport and industry BC (YRE) based on FEG coupling. **a–c** Fraction of province contributions to (a) residential, (b) transport and (c) industry BC. (**d, e, f**) are the SD for data shown in (a, b, c) respectively. Notice that the number in the pie chart represents the percentage (not shown the symbol of %). The seasonal calculations include all samples in the current campaign.

investigations for other megacities in China and South Asia (for example, India and Bangladesh), which are also experiencing severe aerosol pollution^{3,10,14,15,18,19,22,36}, to help frame better policies to tackle air pollution issues synergistically.

Methods

The sampling campaign and concentration analysis. The year-round PM_{2.5} sampling campaigns were simultaneously conducted in urban Shanghai and suburban Chongming Island (YRE; Fig. 1a and Supplementary Fig. 1c). In total, eighty-six urban samples and eighty suburban samples were collected on pre-combusted (500 °C for 6 h) quartz-fiber filters using high-volume samplers with a PM_{2.5} impactor from December 2018 to January 2020. Further detailed information regarding the sampling sites and sampling campaign is available in Supplementary Note 1. The PM_{2.5} concentrations were obtained from mass metrology. The filters were first equilibrated for 48 h in a temperature and humidity-controlled instrument (RH = 50%, T = 25 °C) and then weighed before and after sampling.

The concentrations of OC and BC (here refers to EC, the mass-based analogue of optically-defined BC) were measured by a standard thermal/optical carbon analyzer (Desert Research Institute, DRI Model 2001) using the IMPROVE_A protocol⁴⁸.

As described previously^{22,23}, a fraction of filter samples was extracted by Milli-Q water (resistivity ≥ 18 M Ω -cm) through ultrasonication, centrifugation and filtration of the supernatant using 0.2- μ m cutoff PTFE syringe filters. The water extracts of water-soluble inorganic ions (e.g., potassium) and WSOC (decarbonated by acid) were then analyzed by DIONEX ICS-5000+ SP (Thermo Scientific) and a high-temperature catalytic oxidation instrument (vario TOC select, Elementar Analysensysteme GmbH), respectively. TC, OC and WSOC concentrations were blank corrected by subtracting an average of the field blanks (all the blanks accounted for less than 0.5% of the sample signals). The relative standard deviation of triplicate analysis was <5% for BC, TC, WSOC and K⁺. No BC and K⁺ were detected in the blanks ($n = 12$). In addition, all the instruments were well calibrated by standards and certified reference materials at high frequency (e.g., performed calibration/standard every 5–10 samples) before and during sample analysis.

Dual-carbon isotope analysis. For BC isotope analysis, 16 samples, including 13 YRE samples with relatively high loadings across 4 seasons and 3 urban samples in winter haze, were chosen and isolated for subsequent $\delta^{13}\text{C}$ and $\Delta^{14}\text{C}$ analysis. In principle, at least three representative high-concentration samples (e.g.,

winter haze) were selected for isotope measurement in each quarter (the spring BC only has two isotope data due to one of the BC samples for the isotope measurement failed). The approach of BC isolation by thermal/optical carbon analyzer is similar to the previous studies^{22,28,30,31,36} but with the different states of the isolated BC samples (solid BC isolates in this study), using the different instruments (current DRI vs previous Sunset) and thermal-optical protocols (current IMPROVE_A TOR vs previous NIOSH TOT). Before OCEC analysis and BC isolation, the filter samples were acid-fumigated with 2 M HCl (inside a desiccator for 24 h and subsequently dried at 60 °C for 3 h) to remove carbonates and to prevent their charring effect during pyrolysis^{22,31}. The BC collection is very reliable, and its recovery efficiency is high (the averaged BC recovery efficiency is approximately 87%; Supplementary Table 6 provides the representative recovery efficiency).

For WSOC at YRE, 17 samples, including 7 in winter haze (December–January) and 10 in the other three seasons, were isolated and subjected to carbon isotope analysis. The WSOC isolation method to determine its carbon isotope composition was also described in previous studies^{22,23}. The WSOC extracts were freeze-dried and transferred into carbon-free tin boats and then dried in the oven at 60 °C. In addition, 3 TC samples from wintertime urban haze were selected to perform isotope measurement. The selected 3 BC and 3 TC samples in representative wintertime haze would help compare the current winter urban haze to YRE and the previous BC isotope data in winter urban Shanghai and other megacities in China. Finally, the dried preserved BC, WSOC and TC samples were analyzed for high-precision natural ¹⁴C abundance and ¹³C/¹²C ratio using Accelerator Mass Spectrometry (AMS; i.e., MICADAS, Ionplus AG, Switzerland and 0.5 Mv XCAM, NEC, USA) facility and Isotope Ratio Mass Spectrometer (IRMS). Radiocarbon and stable carbon isotopic values are reported on a per mil scale as $\Delta^{14}\text{C}$ and $\delta^{13}\text{C}$, respectively^{22,23,28,30,31,36,49}. Values of $\delta^{13}\text{C}$ were reported in per mil (‰) relative to the international standards Vienna PeeDee Belemnite (VPDB), and the analytic precision is better than $\pm 0.2\text{‰}$. All $\Delta^{14}\text{C}$ results were corrected for $\delta^{13}\text{C}$ fractionation and for ¹⁴C decay for the time period between 1950 and the year of sample collection. The precision of ¹⁴CO₂ gas measurements for the international standard Oxalic Acid (OxII, NIST SRM 4990 C) is better than 10%. Further detailed carbon isotope measurements, and isotopic results of samples (including BC, WSOC and TC) can be found in Supplementary Note 3 and Table 2, respectively. The field blank filters, plus the laboratory handling sequence and materials used, gave no detectable carbon isotope signal, in line with previous studies^{22,23,28,30,31}.

The relative contributions to atmospheric BC, WSOC and TC from contemporary biomass/biogenic (f_{bio} for WSOC and TC, f_{bb} for BC) sources and radiocarbon-extinct fossil (f_{fossil}) sources can be calculated with an isotopic mass balance equation^{22,23,28,30,31}:

$$\Delta^{14}\text{C}_{\text{sample}} = \Delta^{14}\text{C}_{\text{bio}}f_{\text{bio}} + \Delta^{14}\text{C}_{\text{fossil}}(1 - f_{\text{bio}}) \quad (1)$$

where $\Delta^{14}\text{C}_{\text{sample}}$ represents the radiocarbon signature of a sample (e.g., BC, WSOC and TC), $\Delta^{14}\text{C}_{\text{bio}}$ is the endmember of the contemporary radiocarbon, and $\Delta^{14}\text{C}_{\text{fossil}}$ is defined as -1000‰ , since fossil fuel is completely devoid of ¹⁴C. The contemporary $\Delta^{14}\text{C}_{\text{bio}}$ signature depends on the biomass type, age and year of harvest. The $\Delta^{14}\text{C}$ signatures of atmospheric CO₂ are around $+50\text{‰}$ (that is, applicable for crop residue burning)⁵⁰. In China, freshly younger biomass (e.g., crop residual and younger wood burning) is dominant and $\Delta^{14}\text{C}_{\text{bio}} = +70 \pm 35\text{‰}$ is determined by combining EIs with endmember differences in biomass (see Supplementary Table 7 for $\Delta^{14}\text{C}_{\text{bio}}$ determination). The conservative estimates for combined uncertainties of

endmember and ¹⁴C measurement introduced an f_{bb} variability of $<5\%$.

Monte Carlo (MC) simulations. The dual-carbon isotope signatures of BC were used in combination with our MC method to further constrain the relative contributions from three combustion sources: biomass (f_{bio}), coal (f_{coal}) and liquid fossil fuel ($f_{\text{liq fossil}}$). The isotopic mass balance is described by the following relation^{22,28,30,31}:

$$\begin{pmatrix} \Delta^{14}\text{C}_{\text{sample}} \\ \delta^{13}\text{C}_{\text{sample}} \\ 1 \end{pmatrix} = \begin{pmatrix} \Delta^{14}\text{C}_{\text{bio}} & \Delta^{14}\text{C}_{\text{liq fossil}} & \Delta^{14}\text{C}_{\text{coal}} \\ \delta^{13}\text{C}_{\text{bio}} & \delta^{13}\text{C}_{\text{liq fossil}} & \delta^{13}\text{C}_{\text{coal}} \\ 1 & 1 & 1 \end{pmatrix} \cdot \begin{pmatrix} f_{\text{bio}} \\ f_{\text{liq fossil}} \\ f_{\text{coal}} \end{pmatrix} \quad (2)$$

Here, f is the fractional contribution of a given source, and subscripts of “sample”, “bio”, “liq fossil” and “coal” denote the investigated sample, biomass, liquid fossil and coal respectively. The last row ensures the mass-balance principle. The $\delta^{13}\text{C}$ endmembers for these three source categories were well-established in the literatures^{22,30,31}. Supplementary Table 3 provides source signatures (fuel endmembers, mean \pm SD) of radiocarbon $\Delta^{14}\text{C}$ and stable carbon $\delta^{13}\text{C}$ used in the MC simulation. The MC calculations were performed using the measured $\Delta^{14}\text{C}$ and $\delta^{13}\text{C}$ data, the fuel endmembers and Eq. (2) with 100,000 iterations. The MC numerical simulations outputted the posterior probability density functions (PDF) of the relative source contribution of three major sources (liquid fossil, coal and biomass) for BC aerosols. The mean modelled fraction of the relative source contribution and the numerical spread (normal distribution) can be derived from this PDF (frequency ≥ 0), allowing the computation of the mean and SD of the modelled sources.

FLEXPART-ECLIPSE-GFED transport modelling. To simulate the BC concentrations arriving at YRE, the FLEXPART-ECLIPSE-GFED (FEG) model was used, comprising of the atmospheric dispersion model FLEXPART version 10.4^{40,51,52}, coupled with the ECLIPSE version 6B¹⁵ EI and satellite-based open fire emissions by GFED version 4.1s⁴². FLEXPART version 10.4 ran in backward mode from the station location at YRE and for the exact same periods as the measurements. A mean particulate diameter of 250 nm was used, with a logarithmic size distribution of 0.3. Simulations extended 30 days back in time, which is sufficient to include most emissions injected into an air mass arriving at the station, given a typical BC lifetime of roughly a week. The simulations used operational meteorological analysis data from the European Centre for Medium-Range Weather Forecasts (ECMWF) at a resolution of $1^\circ \times 1^\circ$ latitude/longitude. FLEXPART accounts for dry deposition and wet scavenging of particles, differentiating between below-cloud and in-cloud scavenging. Anthropogenic BC emissions were received from the ECLIPSE version 6B¹⁵, which is based on the GAINS (greenhouse gas–air pollution interactions and synergies) model⁵³. The emissions were explicitly split between biofuels (modern; e.g., agricultural waste burning) and fossil fuels emissions (Supplementary Table 8). Emissions from agricultural waste burning/wildfires were not accounted for in ECLIPSE EI, and they were adopted from GFED. The most recent version (4.1 s) of GFED was applied⁴². This satellite-based emission inventory was used with daily resolution, while the spatial resolution was $0.5^\circ \times 0.5^\circ$ to match ECLIPSE’s resolution.

Data availability

The observational (measurement) data that support the findings of this study are provided in SI. The MC results and the outputs and figures of FEG model simulation are

archived on the Zenodo repository (<https://doi.org/10.5281/zenodo.8010393>). The surface PM_{2.5} observational data from the Chinese Ministry of Ecology and Environment can be obtained from <https://quotsoft.net/air/>. EI data for GFED is freely available and can be found on the website www.globalfiredata.org/data.html. The data for BC emissions for different emission scenarios of ECLIPSE is freely available from IIASA (<https://iiasa.ac.at>).

Code availability

The FLEXPART model is freely available to the scientific community and can be downloaded from <https://www.flexpart.eu/>. Meteorological fields to run FLEXPART can be downloaded from ECMWF (<https://www.ecmwf.int>) following their terms/guidelines.

Received: 23 February 2023; Accepted: 25 August 2023;

Published online: 05 September 2023

References

- Qiao, L. et al. PM_{2.5} constituents and hospital emergency-room visits in Shanghai, China. *Environ. Sci. Technol.* **48**, 10406–10414 (2014).
- An, J. et al. Emission inventory of air pollutants and chemical speciation for specific anthropogenic sources based on local measurements in the Yangtze River Delta region, China. *Atmos. Chem. Phys.* **21**, 2003–2025 (2021).
- New WHO Global air quality guidelines. WHO <https://www.who.int/news/item/22-09-2021-new-who-global-air-quality-guidelines-aim-to-save-millions-of-lives-from-air-pollution> (accessed November 2022).
- Geng, G. et al. Drivers of PM_{2.5} air pollution deaths in China 2002–2017. *Nat. Geosci.* **14**, 645–650 (2021).
- Zhang, Q. et al. Drivers of improved PM_{2.5} air quality in China from 2013 to 2017. *Proc. Natl Acad. Sci. USA* **116**, 24463–24469 (2019).
- Zhai, S. et al. Control of particulate nitrate air pollution in China. *Nat. Geosci.* **14**, 389–395 (2021).
- Zheng, B. et al. Trends in China's anthropogenic emissions since 2010 as the consequence of clean air actions. *Atmos. Chem. Phys.* **18**, 14095–14111 (2018).
- Cai, S. et al. Impact of air pollution control policies on future PM_{2.5} concentrations and their source contributions in China. *J. Environ. Manage.* **227**, 124–133 (2018).
- Li, J. et al. Winter particulate pollution severity in North China driven by atmospheric teleconnections. *Nat. Geosci.* **15**, 349–355 (2022).
- The 17 Sustainable Development Goals (SDGs) in the 2030 Agenda for Sustainable Development* (United Nations, <https://sdgs.un.org/goals>)
- Shindell, D. et al. Simultaneously mitigating near-term climate change and improving human health and food security. *Science* **335**, 183–189 (2012).
- Ebenstein, A. et al. New evidence on the impact of sustained exposure to air pollution on life expectancy from China's Huai River Policy. *Proc. Natl Acad. Sci. USA* **113**, 10384–10389 (2016).
- Tan, Y., Dion, E. & Monteiro, A. Haze smoke impacts survival and development of butterflies. *Sci. Rep.* **8**, 15667 (2018).
- Lu, Z., Zhang, Q. & Streets, D. G. Sulfur dioxide and primary carbonaceous aerosol emission trends in China and India, 1996–2010. *Atmos. Chem. Phys.* **11**, 9839–9864 (2011).
- Klimont, Z. et al. Global anthropogenic emissions of particulate matter including black carbon. *Atmos. Chem. Phys.* **17**, 8681–8723 (2017).
- Zhao, Y. et al. Quantifying the uncertainties of a bottom-up emission inventory of anthropogenic atmospheric pollutants in China. *Atmos. Chem. Phys.* **11**, 4825–4841 (2011).
- Chang, Y. et al. Assessment of carbonaceous aerosols in Shanghai, China – Part 1: long-term evolution, seasonal variations, and meteorological effects. *Atmos. Chem. Phys.* **17**, 9945–9964 (2017).
- Ramanathan, V. & Carmichael, G. Global and regional climate changes due to black carbon. *Nat. Geosci.* **1**, 221–227 (2008).
- Bond, T. C. et al. Bounding the role of black carbon in the climate system: a scientific assessment. *J. Geophys. Res. Atmos.* **118**, 5380–4496 (2013).
- Naik, V. et al. Short-Lived Climate Forcers. In: *Climate Change 2021: The Physical Science Basis. Contribution of Working Group I to the Sixth Assessment Report of the Intergovernmental Panel on Climate Change* (Cambridge University, in Press)
- Andreae, M. O. & Gelencser, A. Black carbon or brown carbon? The nature of the light-absorbing carbonaceous aerosols. *Atmos. Chem. Phys.* **6**, 3131–3148 (2006).
- Fang, W. et al. Divergent evolution of carbonaceous aerosols during dispersal of East Asian haze. *Sci. Rep.* **7**, 10422 (2017).
- Kirillova, E. et al. Sources and light absorption of water-soluble organic carbon aerosols in the outflow from northern China. *Atmos. Chem. Phys.* **14**, 1413–1422 (2014).
- Yan, C. et al. Important fossil source contribution to brown carbon in Beijing during winter. *Sci. Rep.* **7**, 43182 (2017).
- Fang, W. et al. Combined influences of sources and atmospheric bleaching on light absorption of water-soluble brown carbon aerosols. *NPJ Clim. Atmos. Sci.* **6**, 104 (2023).
- Eckhardt, S. et al. Current model capabilities for simulating black carbon and sulfate concentrations in the Arctic atmosphere: a multi-model evaluation using a comprehensive measurement data set. *Atmos. Chem. Phys.* **15**, 9413–9433 (2015).
- Stohl, A. et al. Black carbon in the Arctic: the underestimated role of gas flaring and residential combustion emissions. *Atmos. Chem. Phys.* **13**, 8833–8855 (2013).
- Winiger, P. et al. Siberian Arctic black carbon sources constrained by model and observation. *Proc. Natl Acad. Sci. USA* **114**, E1054–E1061 (2017).
- Wang, H. et al. Health benefits of on-road transportation pollution control programs in China. *Proc. Natl Acad. Sci. USA* **117**, 25370–25377 (2020).
- Andersson, A. et al. Regionally-varying combustion sources of the January 2013 severe haze events over eastern China. *Environ. Sci. Technol.* **49**, 2038–4496 (2015).
- Fang, W. et al. Dual-isotope constraints on seasonally resolved source fingerprinting of black carbon aerosols in sites of the four emission hot spot regions of China. *J. Geophys. Res. Atmos.* **123**, 11735–11747 (2018).
- Stohl, A. et al. Evaluating the climate and air quality impacts of short-lived pollutants. *Atmos. Chem. Phys.* **15**, 10529–10566 (2015).
- Zhang, Y. et al. Fossil vs. non-fossil sources of fine carbonaceous aerosols in four Chinese cities during the extreme winter haze episode of 2013. *Atmos. Chem. Phys.* **15**, 1299–1312 (2015).
- Fang, W. et al. Measurements of secondary organic aerosol formed from OH-initiated photo-oxidation of isoprene using on-line photoionization aerosol mass spectrometry. *Environ. Sci. Technol.* **46**, 3898–3904 (2012).
- Andreae, M. O. Emission of trace gases and aerosols from biomass burning – an updated assessment. *Atmos. Chem. Phys.* **19**, 8523–8546 (2019).
- Bikkina, S. et al. Air quality in megacity Delhi affected by countryside biomass burning. *Nat. Sustain.* **2**, 200–205 (2019).
- Sheehan, P., Cheng, E., English, A. & Sun, F. China's response to the air pollution shock. *Nat. Clim. Chang.* **4**, 306–309 (2014).
- Liu, Z. et al. A low-carbon road map for China. *Nature* **484**, 143–145 (2013).
- Guenther, A. et al. A global model of natural volatile organic compound emission. *J. Geophys. Res. Atmos.* **100**, 8873–8892 (1995).
- Pisso, I. et al. The Lagrangian particle dispersion model FLEXPART version 10.4. *Geosci. Model Dev.* **12**, 4955–4997 (2019).
- Evangelou, N. et al. Wildfires in northern Eurasia affect the budget of black carbon in the Arctic—A 12-year retrospective synopsis (2002–2013). *Atmos. Chem. Phys.* **16**, 7587–7604 (2016).
- van der Werf, G. R. et al. Global fire emissions estimates during 1997–2016. *Earth Syst. Sci. Data* **9**, 697–720 (2017).
- Liu, J. et al. Air pollutant emissions from Chinese households: a major and underappreciated ambient pollution source. *Proc. Natl Acad. Sci. USA* **113**, 7756–7761 (2016).
- Wang, R. et al. Exposure to ambient black carbon derived from a unique inventory and high-resolution model. *Proc. Natl Acad. Sci. USA* **111**, 2459–2463 (2014).
- Zhang, J. et al. Potential role of natural gas infrastructure in China to supply low-carbon gases during 2020–2050. *Appl. Energy* **306**, 117989 (2022).
- Gan, Y. et al. Carbon footprint of global natural gas supplies to China. *Nat. Commun.* **11**, 1–9 (2020).
- Gas Pricing and Regulation: China's Challenges and IEA Experiences (IEA 2012).
- Chow, J. C. et al. Equivalence of elemental carbon by Thermal/Optical Reflectance and Transmittance with different temperature protocols. *Environ. Sci. Technol.* **38**, 4414–4422 (2004).
- Qi, Y. et al. Dissolved black carbon is not likely a significant refractory organic carbon pool in rivers and oceans. *Nat. Commun.* **11**, 5051 (2020).
- Graven, H. D., Guilderson, T. P. & Keeling, R. F. Observations of radiocarbon in CO₂ at seven global sampling sites in the Scripps flask networks: Analysis of spatial gradients and seasonal cycles. *J. Geophys. Res.* **117**, D02302 (2012).
- Stohl, A. et al. Validation of the Lagrangian particle dispersion model FLEXPART against large-scale tracer experiment data. *Atmos. Environ.* **32**, 4245–4264 (1998).
- Stohl, A. et al. Technical note: the Lagrangian particle dispersion model FLEXPART version 6.2. *Atmos. Chem. Phys.* **5**, 4739–4799 (2005).
- Amann, M. et al. Cost-effective control of air quality and greenhouse gases in Europe: modeling and policy applications. *Environ. Model. Softw.* **26**, 1489–1501 (2011).

Acknowledgements

We thank Yepeng Yu, Xuan Lin, Hui Yi, Juan Wang, Kun Wu, Chunle Luo, Zicheng Wang and Xiaoyan Ning for assistance during experiments. Örjan Gustafsson, Xuchen

Wang, August Andersson and Chaeyoon Cho are acknowledged for numerous helpful discussions. The research was funded based on East China Normal University. W.F. acknowledges the start-up funding from East China Normal University. N.E. and S.E. were supported by COMBAT project funded by ROMFORSK of the Research Council of Norway (Project ID: 275407). M.Z. was supported by the funds from the National Natural Science Foundation of China (Grant #42230412 to M.Z.) and acknowledge the OUC-CAMS facility for isotope analysis (#11). We gratefully acknowledge AMS system in CIGG of the Qingdao National Laboratory for Marine Science and Technology (QNLN) in Qingdao in China for TC isotope measurements. The authors also gratefully acknowledge ECMWF for permitting access to the meteorological data used for the model simulations.

Author contributions

W.F. designed the research, performed year-round sampling campaigns and sample analysis. J.X. was involved in experiments. W.F. analyzed and interpreted data with discussion from N.E., S.E., M.Z. and S.K. H.Z. assisted with isotope analysis. W.F. performed MC simulations, while N.E. and S.E. were in charge of FEG simulations. W.F. wrote the paper and produced the figures with input from N.E., S.E., H.X., M.Z. and S.K.

Competing interests

The authors declare no competing interests.

Additional information

Supplementary information The online version contains supplementary material available at <https://doi.org/10.1038/s43247-023-00979-z>.

Correspondence and requests for materials should be addressed to Wenzheng Fang, Sabine Eckhardt or Meixun Zhao.

Peer review information *Communications Earth & Environment* thanks the anonymous reviewers for their contribution to the peer review of this work. Primary Handling Editors: Tuija Jokinen, Joe Aslin and Clare Davis. A peer review file is available.

Reprints and permission information is available at <http://www.nature.com/reprints>

Publisher's note Springer Nature remains neutral with regard to jurisdictional claims in published maps and institutional affiliations.



Open Access This article is licensed under a Creative Commons Attribution 4.0 International License, which permits use, sharing, adaptation, distribution and reproduction in any medium or format, as long as you give appropriate credit to the original author(s) and the source, provide a link to the Creative Commons licence, and indicate if changes were made. The images or other third party material in this article are included in the article's Creative Commons licence, unless indicated otherwise in a credit line to the material. If material is not included in the article's Creative Commons licence and your intended use is not permitted by statutory regulation or exceeds the permitted use, you will need to obtain permission directly from the copyright holder. To view a copy of this licence, visit <http://creativecommons.org/licenses/by/4.0/>.

© The Author(s) 2023